Results in Engineering 26 (2025) 105303

Contents lists available at ScienceDirect

Results in Engineering

journal homepage: www.sciencedirect.com/journal/results-in-engineering

Research paper

Exploring short crack behaviour and fracture transition in 5052 aluminium alloy

Abdalrhaman Koko [a,b,*], Duaa Salim [c], Nathanael Leung [d], Nassos Spetsieris [a], Stan Smith [a], David England [a,d], Tan Sui [a,d], Tony Fry [a]

[a] National Physical Laboratory, Hampton Road, Teddington TW11 0LW, UK
[b] Department of Materials, University of Oxford, Parks Road, Oxford OX1 3PH, UK
[c] Physics Department, University of Khartoum, Khartoum, Sudan
[d] School of Mechanical Engineering Sciences, University of Surrey, Surrey, GU2 7XH, UK

ARTICLE INFO

Keywords:
5052 aluminium alloy
Crack propagation
Stress intensity factor
Digital image correlation
Microstructure-sensitive fracture

ABSTRACT

This study, employing in-situ scanning electron microscopy, electron backscatter diffraction, and digital image correlation, investigates the crack-length dependency of the quasi-brittle to ductile transition in 5052 aluminium alloy. A compact tension sample with {110} texture was examined, revealing crack propagation on $(11\overline{1})$ and $(\overline{1}11)$ transgranular cleavage planes and non-coherent paths under low-stress intensity factors (SIFs), with a maximum of 7.72 ± 0.09 $\text{MPa.m}^{0.5}$ compared to the typical K_{IC} of 25 $\text{MPa.m}^{0.5}$. Crack growth was influenced by double-slip mechanisms and significant resistance at Σ33 grain boundaries. After crack arrest, SIFs derived from the local displacement field revealed a transition from microstructure-sensitive to nominal load-driven crack growth conditions.

1. Introduction

Ensuring the safety and reliability of structural materials remains a critical challenge, particularly in understanding crack propagation mechanisms that ultimately dictate material failure [1–4]. Cracks spend a significant portion of their lifetime at the microstructural scale, where far-field applied stresses do not merely govern them but are strongly influenced by local features such as grain boundaries, crystallographic orientations, and micro-scale residual stresses [5–7]. At this scale, cracks exhibit tortuous growth paths and highly variable propagation rates as they traverse individual grains [8,9]. These short cracks, with lengths on the order of a few grains, behave unpredictably compared to longer cracks, due to their strong sensitivity to the underlying microstructure as the interplay introduces localised stress concentrations, crack deflection, and plasticity, significantly complicating crack growth predictions [10,11].

Although similar sensitivity has been observed in various ductile metals, including magnesium [12], nickel [13,14], and titanium [15,16]; it is generally attributed to geometry, morphology, and sometimes dislocation activities [17,18]. Aluminium alloys are well-known for their ductility and high fracture toughness [19,20]; however, their crack growth at the micro-scale is generally not well studied, and ductile tearing is typically accepted as the mechanism for crack propagation. Most experimental research on short crack growth in aluminium alloys has focused on fatigue crack propagation, with limited attention given to quasi-static loading conditions [21,22]. Studies on high-strength aluminium alloys such as AA-2024 and AA-7075 have shown that short cracks frequently arrest at grain boundaries or secondary phase particles before transitioning to a more stable propagation mode. However, the crack growth mechanisms in highly ductile aluminium alloys remain less well understood, highlighting the need for further exploration of plasticity-driven crack propagation.

5xxx series aluminium alloys, recognised for their exceptional ductility and fracture toughness, are widely utilised in aerospace, automotive, and marine applications. Despite their widespread use, the short crack growth behaviour of these alloys at the microscale remains inadequately studied. While ductile tearing is commonly accepted as the primary crack propagation mechanism [23–26], the transition from quasi-brittle behaviour to ductile tearing requires further investigation. This transition is especially relevant for structural integrity assessment and material processing optimisation. However, limited research has been conducted to identify the specific factors that govern this transition

---

[*] Corresponding author at: National Physical Laboratory, Hampton Road, Teddington TW11 0LW, UK.
E-mail address: abdo.koko@npl.co.uk (A. Koko).

https://doi.org/10.1016/j.rineng.2025.105303
Received 17 March 2025; Received in revised form 28 April 2025; Accepted 11 May 2025

in short cracks, particularly in AA-5052. Recent studies examining monotonic tensile loading of AA-5052 have revealed intricate crack propagation behaviours during the early stages of fracture [27–29], underscoring the need to distinguish the influence of microstructural features from global stress states. Additionally, residual stresses introduced by cold working and strain hardening further complicate the analysis of crack growth dynamics.

Understanding short crack propagation in AA-5052 is essential for improving the performance and reliability of components exposed to high-stress conditions, such as those in aerospace and automotive applications [27]. Short cracks, defined as those with lengths comparable to or smaller than the grain size, pose a significant challenge because their growth cannot be accurately described using traditional linear elastic fracture mechanics [13]. Unlike long cracks, which propagate in accordance with stress intensity factors, short cracks are heavily influenced by microstructural heterogeneities, including grain boundaries and phase interfaces [18]. Prior studies have shown that AA-5052's microstructural characteristics, including grain size, phase distribution, and strain-hardening behaviour, significantly affect its fracture response [30]. Research on fatigue crack growth in aluminium alloys, including AA-5052, has demonstrated that local microstructural variations can lead to unpredictable crack propagation, blunting, or even arrest [31]. Consequently, a comprehensive understanding of short crack behaviour is necessary to improve fatigue life predictions and prevent unexpected failures in critical structural components.

This study on 5052 aluminium alloys (AA-5052) under monotonic tensile loading has revealed complex crack behaviours, especially in the early stages of fracture, which underlines the need to decouple the influence of microstructural features from global stress states. Here, we attempt to achieve this by mapping the microstructure using electron backscatter diffraction (EBSD), in-situ micro-scale imaging of the crack propagation, and employing digital image correlation (DIC) techniques to measure local stress intensity factors (SIFs) at the crack tip. These findings shed light on the transition of cracks from microstructurally driven growth to a nominal load-driven regime.

2. Methodology

An ASTM E1820 compact tension (CT) sample was fabricated from aerospace-grade AA-5052 aluminium alloy, which has the chemical composition detailed in Table 1. The sample exhibits a {110} crystallographic texture, and the compact tension notch was oriented in alignment with the rolling direction of the material. The CT sample has a thickness (B) of 2.82 ± 0.02 mm, effective width (W) of 13 ± 0.08 mm, notch size of 0.5 W, and a pin diameter of 7.8 mm to promote plane stress conditions (see the supplementary information for more CT sample schematic). The sample was fatigue cycled at 10 Hz and $R = 0.1$ to create a 3.28 ± 0.02 mm sharp crack, then mirror polished.

Gold nanoparticles were synthesised to create a speckle pattern suitable for DIC. This was done by mixing 1 wt% (1 g) of $Na_3C_6H_5O_7$ in 100 ml of deionised (DI) water. Concurrently, 1 g of $HAuCl_4{\cdot}3H_2O$ was dissolved in 250 ml of DI water to make a 10 mM solution. A solution was prepared by mixing 12 ml of the 10 mM $HAuCl_4$ solution with 400 ml of DI water and brought to a boil. To this, 3.2 ml of $Na_3C_6H_5O_7$ was added to achieve a particle size of 40–60 nm. The mixture was boiled until it turned maroon, indicating the formation of gold nanoparticles, and then allowed to cool. For salinization, 50 ml of DI water was added to 47.5 ml of anhydrous ethanol and mixed. Then, 2.5 ml of (3-Aminopropyl)trimethoxysilane was added and mixed. The sample was placed in the mixer for 15 min, then cleaned in ethanol and DI water, and dried with an air blower. Finally, the sample was soaked for 32 h in the gold nanoparticle solution to deposit 40–60 nm nanoparticles, creating the speckle pattern necessary for DIC (Au in Fig. 1) [32,33].

Table 1
Measured chemical composition of the AA-5052 plate in weight %.

Al	Mg	Fe	Cr	Si	Mn	Cu	Zn
Bal.	3.14 ± 0.18	0.36 ± 0.01	0.22 ± 0.08	0.13 ± 0.02	0.05 ± 0.01	0.04 ± 0.01	0.01 ± 0.00

Tensile testing of the speckled CT sample was conducted in a MIRA TESCAN SEM using a 5kN Deben stage at 0.2 mm/min, WD of 14 mm, and 15 keV beam energy. The sample was loaded in x_2 direction (Fig. 1b). The test was periodically paused, holding the sample in displacement control, to monitor crack growth using a backscattered electron (BSE) detector at 15 keV (Fig. 1a and b). The crack was imaged at various magnifications to ensure precise crack length measurement, and facilitate subsequent digital image correlation (Fig. 1c) by exploiting the contrast difference between the aluminium and high-density gold speckles (bright spots in Fig. 1) and AA-5052.

Subsequently, DIC was performed on 500 μm × 500 μm BSE images with a pixel size of 200 nm using DaVis v.10.2 software (LaVision GmbH) following iDICs guidelines [34]. Parameters included a 49-pixel subset size, 32-pixel step size, second-order subset shape function, Zero-Normalised Sum of Squared Differences (ZNSSD) matching, and bicubic spline interpolation. Rigid body movement correction was applied by setting the point of minimum displacement as the origin to isolate material deformation [35].

After testing, the sample was mirror-polished, and the microstructure near the crack was mapped via EBSD using a Zeiss Auriga 60 SEM with an Oxford Symmetry 2 detector. EBSD was conducted at a 14 mm working distance, with a 20 keV electron beam and a 60 μm aperture, collecting data at a 0.5 μm step size.

3. Results and discussion

3.1. Fatigue pre-crack path

The crack path was segmented and analysed with respect to its crystallographic orientation and grain boundary character, as summarised in Table 2 and Fig. 2. Each segment corresponds to a unique grain and is defined by its crack plane, misorientation angle, and the type of coincidence site lattice (CSL) boundary encountered.

Fig. 2 shows that the initial fatigue generated a crack in Grain A via localised splitting (labelled 1-1 and 1-2 in Fig. 2b) and propagated transgranularly along the $(1\bar{1}1) \pm 4.27^\circ$ and $(\bar{1}11) \pm 5.52^\circ$ planes, until reaching Segment 4 (Fig. 2a), where it encountered a $\Sigma 11 \pm 4.15^\circ$ grain boundary. The crack then crosses into Grain B, where it grew over its most extended continuous segment, particularly in Segment 7, before traversing a $\Sigma(29a, 35b) \pm 1.69^\circ$ boundary to enter Grain C. In Grain C, the crack alternated between the $(1\bar{1}1) \pm 2.19^\circ$ and $(\bar{1}11) \pm 1.97^\circ$ planes, inducing significant plastic deformation that fragmented the grain into three sub-regions (Grains C-1, C-2, and C-3). This grain refinement resulted from localised plasticity near the crack tip as it adapts to crystallographic misorientation and slip constraints. A similar fragmentation occurred in Grain D, splitting it into Grains D-1 and D-2 during crack arrest and continued loading. These deformation-induced misorientations and grain refinements remain visible post-polishing for EBSD, despite some alleviation of residual plastic strain.

Although we did not directly measure dislocation density, the observed grain fragmentation and local misorientation gradients in Grains C and D suggest high local plastic deformation, likely linked to elevated dislocation activity at the crack tip. This high dislocation density may have facilitated transgranular propagation along the $(11\bar{1})$ and $(\bar{1}11)$ cleavage planes by enabling shear-dominated fracture. The absence of intergranular crack paths further implies that the GBs in these regions were not significantly weakened, potentially due to lower dislocation pile-up at the boundaries. Quantifying dislocation density, for instance, through HR-EBSD or TEM, would offer valuable insight in future studies.

The crack crosses to Grain D with significant resistance encountered

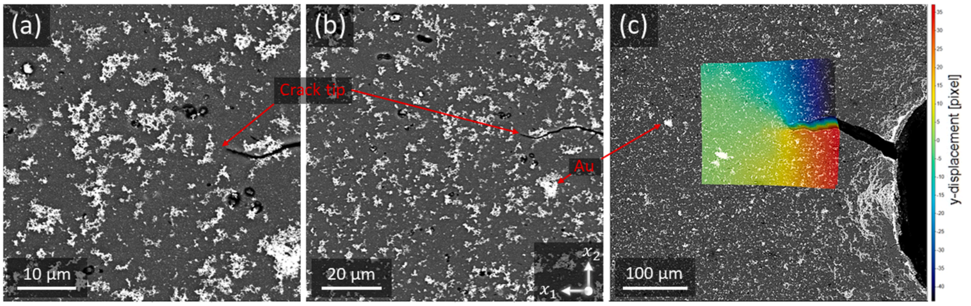

Fig. 1. BSE images of the crack tip: (a-b) crack propagation, and (c) global DIC for local mechanical conditions at the stationary crack.

Table 2
Characteristics of the crack path in the AA-5052 as traced from SEM images and the EBSD map (Fig. 2b) detailing the grain IDs, crack segment lengths as shown in Fig. 2a, crack planes, grain boundary misorientation angles, and probable coincidence site lattice (CSL) boundary types encountered during propagation. For detailed trace analysis, see the supplementary information A.

Segment	Grain ID	Length (µm)	Crack plane	GB (°)	Σ
1	A	11.54 ± 0.69	$(1\bar{1}1)$±4.27°		
2		7.4 ± 0.44	$(\bar{1}11)$ ± 5.52°		
3		10.32 ± 0.52	-		
4		6.13 ± 0.60	$(1\bar{1}1)$ ± 6.14°		
				52.20 ± 4.15	Σ11
5	B	22.72 ± 1.36	-		
6		9.7 ± 0.68	$(\bar{1}11)$ ± 8.58°		
7		33.99 ± 2.72	-		
				42.11 ± 1.69	Σ(29a, 35b)
8	C	8.27 ± 0.74	$(1\bar{1}1)$ ± 2.19°		
9		28.19 ± 1.44	$(\bar{1}11)$ ± 1.97°		
10		14.96 ± 0.90	-		
				57.42 ± 2.77	Σ33c
11	D	13.36 ± 0.94	$(\bar{1}11)$ ± 8.08°		
12		5.58 ± 0.33	$(1\bar{1}1)$ ± 4.24°		

at the Σ33c ± 2.77° grain boundary where the crack deflects. The crack enters Grain D in Segment 11 along $(\bar{1}11)$ ± 8.08° and is eventually arrested after taking $(1\bar{1}1)$ ± 4.24° to in Segment 12. The crack predominantly followed the $(1\bar{1}1)$ and $(\bar{1}11)$ crystallographic cleavage planes for 53 % of its growth, with the remainder propagating along non-coherent cleavage planes, such as in Segment 7.

The non-coherent cleavage plane propagation is consistent with the double-slip mechanism [36], where short cracks propagate via the combined action of two slip systems, resulting in crack extension along non-crystallographic directions. Additionally, GBs act as barriers to dislocation motion, causing dislocation pile-ups at the crack tip and creating localised stress concentrations. This accumulation can promote crack initiation and influence the subsequent propagation path by altering the stress field geometry and enhancing the driving force for transgranular cleavage [37,38]. The increased dislocation density near GBs contributes to higher local resistance, thereby affecting the effective fracture toughness and the observed tortuosity in short crack propagation [39–41]. In our study, the crack's tortuous path highlights the critical role of grain boundaries, particularly Σ33c, as strong barriers to propagation, consistent with energy dissipation mechanisms.

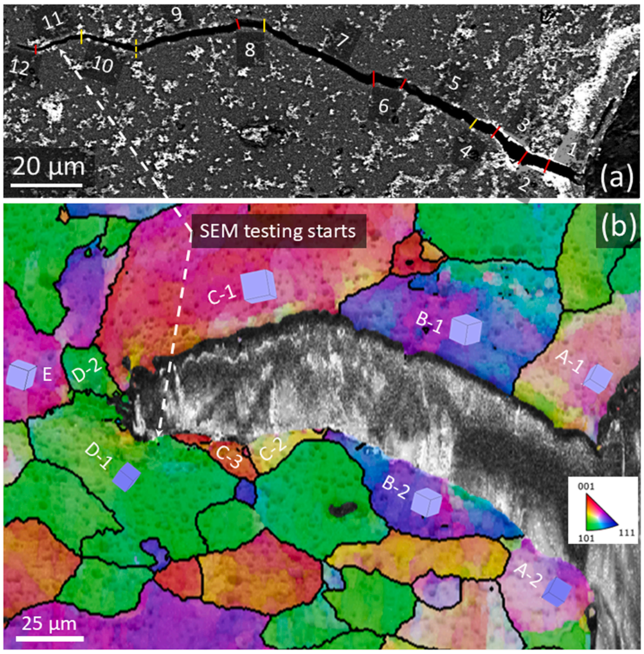

Fig. 2. (a) In-situ BSE image of the crack path at 0.18 mm, showing crack deflection (red) and grain boundary crossings (yellow). (b) Ex-situ EBSD map of the microstructure. Electron shadowing affected EBSD at the edge of Grain C.

3.2. *In-situ crack growth*

The SEM monotonic tensile test began in the region marked in Fig. 2, capturing crack propagation within Grain D (Segments 11 and 12). Fig. 3a shows the corresponding load-displacement curve during this in-situ phase. As load increases, the crack advances from Segment 11 into Segment 12 along the $(1\bar{1}1)$ plane, until it is arrested. The total crack growth from the notch measured 172.16 ± 3.93 µm from the notch with 6.93 ± 0.31 µm tracked directly inside the SEM.

Crack lengths (Fig. 3b) are determined from the in situ SEM images taken at various magnifications, with segmentation and summation performed at low magnification. At higher magnifications, reference points are used to correlate incremental growth by measuring the distance from these points to the crack tip. The crack length (L) is used to calculate the stress intensity factor (SIF, K) using ASTM E1820 (Eq. (1)) [42], where P is the applied load, and a is the crack length. The ASTM-based SIF uncertainty is calculated via the Monte Carlo method (Fig. 3b), and more details about the uncertainty calculation can be

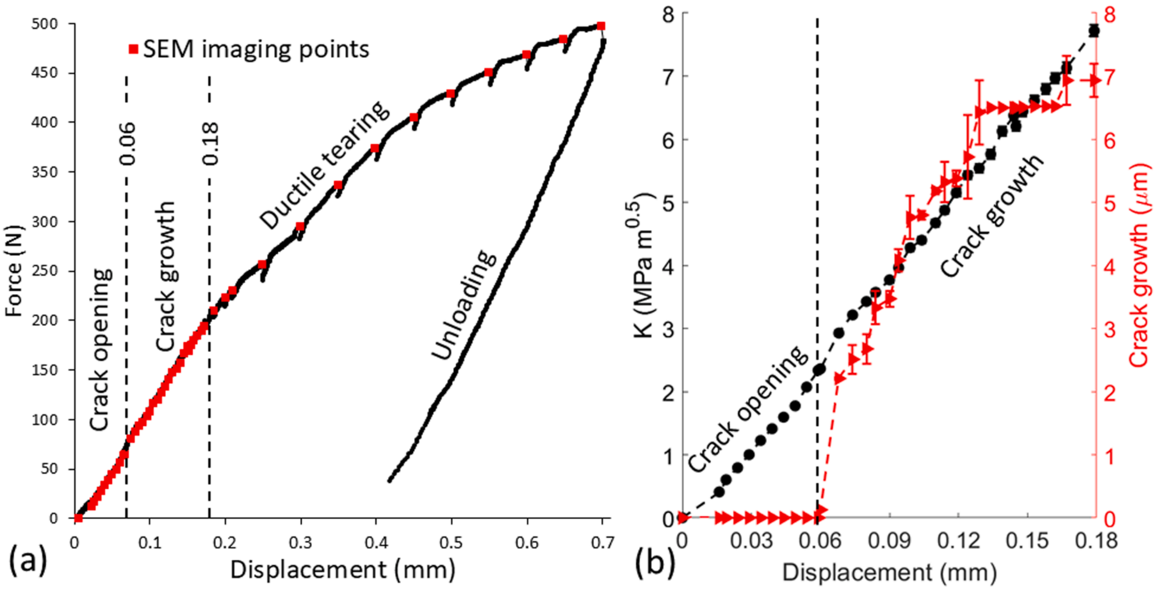

Fig. 3. (a) Load-displacement curve for the in-situ SEM test with red markers indicating imaging points. (b) Measured crack length increments and calculated $\boldsymbol{K}$ up to 0.18 mm.

found in the supplementary information C.

$$K=\frac{P}{BW^{1/2}}\frac{2+a/W}{(1-a/w)^{3/2}}\left[0.886+4.64\left(\frac{a}{W}\right)-13.32\left(\frac{a}{W}\right)^{2}+14.72\left(\frac{a}{W}\right)^{3}-5.6\left(\frac{a}{W}\right)^{4}\right]\because a=0.5W+L \tag{1}$$

The crack propagation within a single grain initially follows a linear regime of the SIF and apparent crack opening, with the surface crack tip advancing as the load increases (Fig. 3b). Up to 0.06 mm straining, the crack continues to open gradually, with a sudden displacement increment of 2.08 ± 0.16 μm. After that, the crack growth increases erratically, corresponding to stable crack growth dominated by the local stress field at the crack tip. During this stage, the crack growth remains nearly proportional to the ASTM-based SIF up to 0.18 mm, within linear elastic fracture mechanics assumptions. Despite jumps in crack length between 0.06 mm and 0.18 mm displacement, these minimally affect the calculated ASTM-based SIF due to its proportion to the notch size; thus, ASM-based SIF remains primarily linear reflecting the elastic relationship between stress and strain and the quasi-brittle crack propagation.

3.3. DIC-based stress intensity factor

Once the crack stopped growing after 0.18 mm displacement, a wide field of view was captured as the load increased for DIC analysis against the image of the loading interval at 0.18 mm (Fig. 1c). A model was created in ABAQUS® v.6.14 using a rectangular grid with 4-node plane stress elements (ABAQUS® CPS4) matched with the DIC grid using a custom-made MATLAB code detailed in [43]. The experimental DIC displacement field was then applied as boundary conditions, and the mode I and II SIFs at the crack tip were calculated using the interaction integral method in ABAQUS® while assuming linear elastic conditions under plane-stress conditions, with Young's modulus of 69.99 ± 0.33 GPa and Poisson's ratio: 0.321 ± 0.005 measured using impact excitation.

The crack direction (q_1) was assumed parallel to the sample x_1-axis in Fig. 1, and the equivalent domain integral (EDI) was defined by an inner contour around the crack tip and outer contours expanding outward in ~2 μm intervals (Fig. 4a). The EDI method allows the determination of the local driving force at the blocked short crack without prior knowledge of theoretical solutions or far-field boundary conditions, and it can be applied to the tip of a tortuous crack by defining an appropriate local frame of reference [44]. Thus, the changes in both

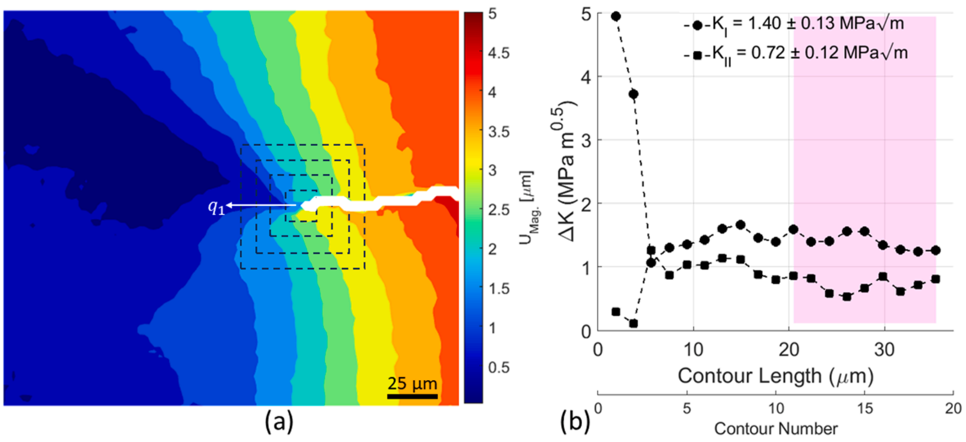

Fig. 4. (a) DIC displacement field at 0.493 mm around the crack (white) with integration domains along $\boldsymbol{q}_1$. (b) Calculated SIFs from the displacement field.

mode I and II SIFs ($\Delta K_{I,II}$) can be extracted from the DIC field using the EDI interaction, which is important as once the crack stopped growing, the linear relationship between the ASTM-based SIF (K) and displacement became parabolic (Fig. 5a), and the crack started to exhibit more elastoplastic behaviour.

The integration domain converges once the singularity ahead of the crack is engulfed (Fig. 4b). Initial non-convergence is due to the breakdown of the elasticity assumption and elevated localised plasticity or poor discretisation of the strain data near the crack tip [45], but stable convergence was achieved as the domain expanded. The characteristic crack opening mode I (ΔK_I) and crack in-plane shear mode II (ΔK_{II}) values are taken from the stable converged region (shaded area in Fig. 4b), with the variance indicating convergence stability.

The normalised DIC-based $\Delta K_{I,II}$ (Fig. 5b) – obtained once the crack was arrested – shows a decreasing ΔK_{II} and increasing ΔK_I, providing insight into the evolving conditions at the crack tip as it transitions from mixed mode microstructurally driven crack to nominal load-driven crack. Initially, when the crack is short and constrained within a grain, its growth is heavily influenced by the local crystallographic orientation and the grain's specific slip system, as described earlier. In addition, the crack was arrested on a coherent cleavage plane similar to an inclined slip plane, as in face-centred cubic materials, such as the aluminium alloy in question, where the slips share the same planes as cleavage planes. This facilitates a shear-dominated crack growth.

In addition, the crack path is tortuous, with the tip being at $14.04 \pm 2.14^\circ$ from the x_1 axes and q_1 direction, which further supports shear-dominated crack conditions at the crack tip. Nonetheless, as the crack grows, it becomes less constrained by the microstructure, and the influence of the globally applied stresses becomes more significant; this shift is marked by an increasing ΔK_I, which signifies that the nominal tensile mode (mode I) is now the dominant driving force as the crack aligns with the principal stress direction, e.g., tensile stress. This transition is consistent with a long crack regime, where the crack responds more predictably to the far-field loading than the localised microstructural features.

4. General discussion

Microstructurally, the crack was arrested inside a grain, and with increasing applied load, further plastic deformation around the crack tip became constrained, resulting in limited slip activity. With increasing straining, the crack tip geometry transitioned from sharp to blunt, forming a stretch zone – a characteristic feature where local plasticity causes material elongation and crack tip blunting under tensile stresses (Fig. 5c, with detailed analysis available in the supplementary information B). In addition, this local plasticity induced a topography to take the shape of an elliptical topographic singularity that starts from the tip, which was also reported recently in [28]. This blunting is associated with reduced stress concentration at the crack tip, temporarily impeding further growth. The crack remains open after removing the load, suggesting significant residual stress and plastic deformation in the surrounding material. This open-crack condition highlights the irreversible plasticity and energy dissipation that occurred during crack propagation and the material's inability to recover elastically due to localised damage.

The crack propagated under a significantly lower SIF compared to the typical fracture toughness of AA-5052, which ranges from 25 to 30 $\text{MPa}\cdot\text{m}^{0.5}$ [46], suggesting it may have originated below the surface, with only a thin surface layer cracking under the lower SIF. However, once the crack ceased to grow, the SIF increased to 18.30 ± 0.22 $\text{MPa}\cdot\text{m}^{0.5}$ by the end of the test. This observation aligns with previous studies suggesting that short cracks typically propagate at much lower stress intensity factors than long cracks [10,18], as a substantial portion of the energy is derived from internal stresses and dislocation structures rather than the energy directly applied within a single cycle [5,47]. On the other hand, fracture toughness is considered a global material property and is typically associated with the behaviour of long cracks. In our experiment, as the applied nominal load increased sufficiently, the arrested crack transitioned into a long crack, demonstrating the material's fracture toughness characteristics.

While tensile residual stresses were not explicitly introduced or measured in this study, we acknowledge that localised residual stress fields may arise from microstructural inhomogeneity and prior plastic deformation near the crack tip, potentially influencing the observed

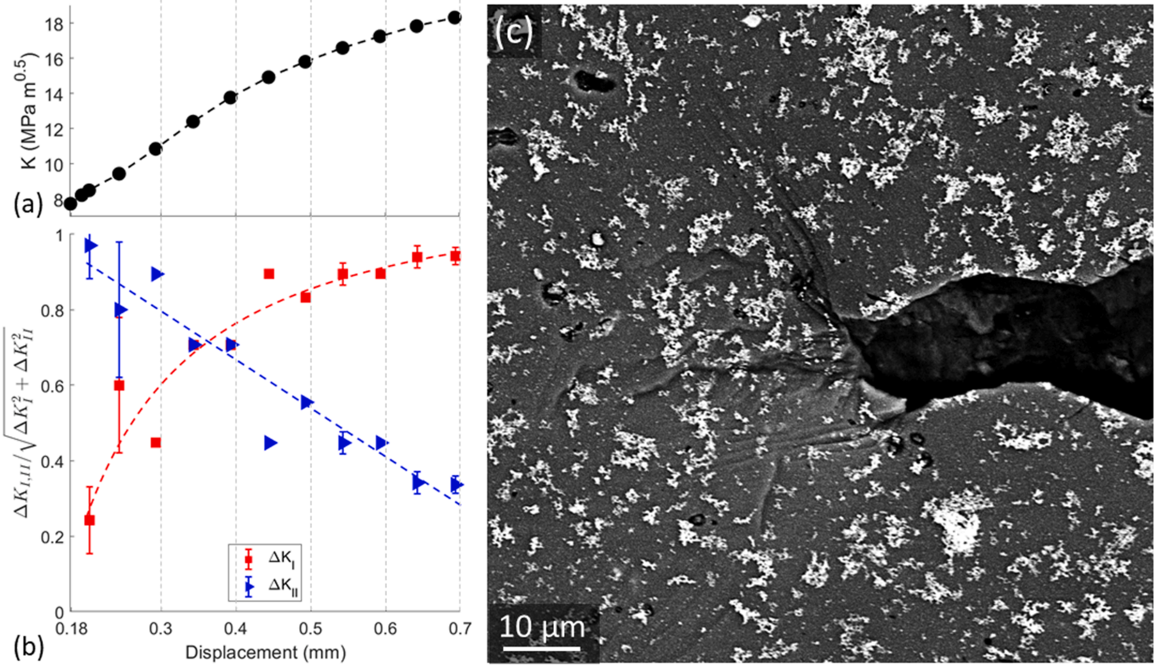

Fig. 5. (a) Analytical $\boldsymbol{K}$ changes and crack increments beyond 0.18 mm strain. (b) Normalised $\boldsymbol{\Delta K_{I,II}}$ from DIC with power law fit for $\boldsymbol{\Delta K_I}$ and linear fit for $\boldsymbol{\Delta K_{II}}$. (c) In-situ image of stationary crack at 0.7 mm.

crack path and local fracture resistance [48–50].

5. Conclusions

This study investigated short crack propagation in AA-5052 under monotonic loading using in-situ SEM, EBSD, and DIC. The results show that crack growth initiates along favoured slip planes, mixed with double slip in non-coherent planes, and is strongly influenced by grain boundaries, particularly Σ33c, which acts as a barrier. Although dislocation density was not directly measured, grain fragmentation suggests significant local plasticity.

The linearity of the analytically calculated stress intensity factor (SIF) during the in-situ crack growth reflects the nominal applied force and the elastic response of the material. However, while the analytical SIF provides a broader approximation of the fracture process based on the nominal load, it is not sensitive to micro-crack propagation or the local driving forces near the crack tip, which was captured via the DIC-derived SIFs. As the crack transitioned from microstructure-sensitive to load-driven growth, we observed a shift in fracture behaviour consistent with quasi-brittle to ductile transition. These findings underline the importance of multiscale approaches in capturing early-stage fracture mechanisms in ductile alloys.

CRediT authorship contribution statement

Abdalrhaman Koko: Writing – original draft, Visualization, Software, Methodology, Investigation, Formal analysis, Conceptualization. **Duaa Salim:** Writing – original draft, Visualization, Investigation, Formal analysis. **Nathanael Leung:** Writing – review & editing, Investigation. **Nassos Spetseieris:** Writing – review & editing, Investigation. **Stan Smith:** Investigation. **David England:** Writing – review & editing, Investigation. **Tan Sui:** Writing – review & editing, Resources. **Tony Fry:** Writing – review & editing, Resources, Funding acquisition.

Declaration of competing interest

The authors declare that they have no known competing financial interests or personal relationships that could have appeared to influence the work reported in this paper.

Acknowledgement

The authors thank Dr Ken Mingard (National Physical Laboratory) for proofreading the article. The authors acknowledge the financial support from the National Measurement System (NMS) programme of the UK government's Department for Science, Innovation and Technology (DSIT), and the Sudanese Materials Scientists and Engineers (SMSE).

Supplementary materials

Supplementary material associated with this article can be found, in the online version, at doi:10.1016/j.rineng.2025.105303.

Data availability

Data will be made available on request.

References

[1] J.H. Chen, R. Cao, Micromechanism of Cleavage Fracture of Metals, 1st ed., Elsevier, Oxford, 2015 https://doi.org/10.1016/C2013-0-18727-2.

[2] M. Badaruddin, S.S. Sugiyanto, D. Asmi, Improvement of the fatigue crack growth resistance in AISI 4140 steel under single- and multi-austempering heat treatments, Results Eng. 21 (2024) 101814, https://doi.org/10.1016/j.rineng.2024.101814.

[3] J. Marrow, D. Scotson, X. Jin, H. Chen, Y. Chen, A. Koko, et al., Small-specimen testing, with image-based analysis, for crack propagation resistance in polygranular nuclear graphite. Graphite Testing for Nuclear Applications: The Validity and Extension of Test Methods for Material Exposed to Operating Reactor Environments, ASTM International, 2022, pp. 1–17, https://doi.org/10.1520/STP163920210051, 100 Barr Harbor Drive, PO Box C700, West Conshohocken, PA 19428-2959.

[4] A. Koko, S. Singh, S. Barhli, T. Connolley, N.T. Vo, T. Wigger, et al., 3-Dimensional analysis of fatigue crack fields and crack growth by in situ synchrotron X-ray tomography, Int. J. Fatigue 170 (2023) 107541, https://doi.org/10.1016/j.ijfatigue.2023.107541.

[5] K. Sadananda, A.K. Vasudevan, Short crack growth and internal stresses, Int. J. Fatigue 19 (1997) 99–108, https://doi.org/10.1016/S0142-1123(97)00057-1.

[6] T. Zhai, A.J. Wilkinson, J.W. Martin, A crystallographic mechanism for fatigue crack propagation through grain boundaries, Acta Mater. 48 (2000) 4917–4927, https://doi.org/10.1016/S1359-6454(00)00214-7.

[7] A. Koko, T.H. Becker, E. Elmukashfi, N.M. Pugno, A.J. Wilkinson, T.J. Marrow, HR-EBSD analysis of in situ stable crack growth at the micron scale, J. Mech. Phys. Solids 172 (2023) 105173, https://doi.org/10.1016/j.jmps.2022.105173.

[8] D.L. McDowell, F.P.E. Dunne, Microstructure-sensitive computational modeling of fatigue crack formation, Int. J. Fatigue 32 (2010) 1521–1542, https://doi.org/10.1016/j.ijfatigue.2010.01.003.

[9] V. Prithivirajan, P. Ravi, D. Naragani, M.D. Sangid, Direct comparison of microstructure-sensitive fatigue crack initiation via crystal plasticity simulations and in situ high-energy X-ray experiments, Mater. Des. 197 (2021) 109216, https://doi.org/10.1016/J.MATDES.2020.109216.

[10] D. Wilson, F.P.E. Dunne, A mechanistic modelling methodology for microstructure-sensitive fatigue crack growth, J. Mech. Phys. Solids 124 (2019) 827–848, https://doi.org/10.1016/j.jmps.2018.11.023.

[11] H. Jin, W.-Y. Lu, S. Haldar, H.A. Bruck, Microscale characterization of granular deformation near a crack tip, J. Mater. Sci. 46 (2011) 6596–6602, https://doi.org/10.1007/s10853-011-5608-3.

[12] Y. Nakai, M. Saka, H. Yoshida, K. Asayama, S. Kikuchi, Fatigue crack initiation site and propagation paths in high-cycle fatigue of magnesium alloy AZ31, Int. J. Fatigue 123 (2019) 248–254, https://doi.org/10.1016/j.ijfatigue.2019.02.024.

[13] Y. Gao, J.S. Stölken, M. Kumar, R.O. Ritchie, High-cycle fatigue of nickel-base superalloy René 104 (ME3): interaction of microstructurally small cracks with grain boundaries of known character, Acta Mater. 55 (2007) 3155–3167, https://doi.org/10.1016/j.actamat.2007.01.033.

[14] T. Zhang, J. Jiang, B.A. Shollock, B.T. Ben, F.P.E. Dunne, Slip localization and fatigue crack nucleation near a non-metallic inclusion in polycrystalline nickel-based superalloy, Mater. Sci. Eng.: A 641 (2015) 328–339, https://doi.org/10.1016/J.MSEA.2015.06.070.

[15] Y. Xu, S. Joseph, P. Karamched, K. Fox, D. Rugg, F.P.E. Dunne, et al., Predicting dwell fatigue life in titanium alloys using modelling and experiment, Nat. Commun. 11 (2020) 5868, https://doi.org/10.1038/s41467-020-19470-w.

[16] C. Liu, R. Thomas, J. Quinta da Fonseca, M. Preuss, Early slip activity and fatigue crack initiation of a near alpha titanium alloy, MATEC Web Conf. 321 (2020) 11040, https://doi.org/10.1051/matecconf/202032111040.

[17] B. Chen, J. Jiang, F.P.E. Dunne, Is stored energy density the primary meso-scale mechanistic driver for fatigue crack nucleation? Int. J. Plast 101 (2018) 213–229, https://doi.org/10.1016/J.IJPLAS.2017.11.005.

[18] D. Wilson, Z. Zheng, F.P.E. Dunne, A microstructure-sensitive driving force for crack growth, J. Mech. Phys. Solids 121 (2018) 147–174, https://doi.org/10.1016/j.jmps.2018.07.005.

[19] A. Alssayegh, M.Y. Abdellah, M.K. Hassan, S. Azam, A. Melaibari, U.A. Khashaba, Optimizing high cycle fatigue predictions in notched Al 7075-T6: an analytical approach to rotating bending behavior, Results Eng. 25 (2025) 103623, https://doi.org/10.1016/j.rineng.2024.103623.

[20] Hendrato, P. Puspitasari, T. Jamasri, Fatigue crack growth rate and mechanical properties of one-step double-side friction stir welded AA6061-T6, Results Eng. 21 (2024) 101958, https://doi.org/10.1016/j.rineng.2024.101958.

[21] Y. Murakami, K. Takahashi, K. Toyama, Mechanism of crack path morphology and branching from small fatigue cracks under mixed loading, Fatigue Fract. Eng. Mater. Struct. 28 (2005) 49–60, https://doi.org/10.1111/j.1460-2695.2004.00828.x.

[22] H. Coules, M. Probert, K. Azuma, C. Truman, C.E. Seow, T. Pirling, et al., Subsurface fatigue crack tip strains in 7475-T7351 aluminium alloy measured using stroboscopic neutron diffraction, Fatigue Fract. Eng. Mater. Struct. 46 (2023) 1735–1749, https://doi.org/10.1111/ffe.13955.

[23] G. Zhao, M. Sun, J. Li, H. Li, L. Ma, Y. Li, Study on quasi-in-situ tensile microstructure evolution law of 5052-O aluminum alloy based on EBSD, Mater. Today Commun. 33 (2022) 104572, https://doi.org/10.1016/j.mtcomm.2022.104572.

[24] V. Espeseth, D. Morin, C. Tekoğlu, T. Børvik, O.S. Hopperstad, Ductile tearing of aluminium plates: experiments and modelling, Int. J. Fract. 242 (2023) 39–70, https://doi.org/10.1007/s10704-023-00701-2.

[25] L. Ma, Y. Deng, Y. Ren, W. Hu, Influence of orientation on crack propagation of aluminum by molecular dynamics, Eur. Phys. J. B 95 (2022) 25, https://doi.org/10.1140/epjb/s10051-022-00285-1.

[26] V. Yamakov, E. Saether, E. Glaessgen, A continuum-atomistic analysis of transgranular crack propagation in aluminum, in: 50th AIAA/ASME/ASCE/AHS/ASC Structures, Structural Dynamics, and Materials Conference, American Institute of Aeronautics and Astronautics, Reston, Virigina, 2009, https://doi.org/10.2514/6.2009-2587.

[27] I.V. Lomakin, T. Mäkinen, K. Widell, J. Savolainen, S. Coffeng, J. Koivisto, et al., Fatigue crack growth in an aluminum alloy: avalanches and coarse graining to

growth laws, Phys. Rev. Res. 3 (2021) L042029, https://doi.org/10.1103/PhysRevResearch.3.L042029.

[28] M. Gattu, S. Aala, Size-effect method to determine mode-I fracture toughness of aluminium alloys, Eng. Fract. Mech. 242 (2021) 107504, https://doi.org/10.1016/j.engfracmech.2020.107504.

[29] T. Soysal, S. Kou, Solidification cracking test of aluminium alloy 5052, Sci. Technol. Weld. Join. 27 (2022) 301–308, https://doi.org/10.1080/13621718.2022.2051410.

[30] J. Fang, Z. Zhu, X. Zhang, L. Xie, Z. Huang, Tensile deformation and fracture behavior of AA5052 aluminum alloy under different strain rates, J. Mater. Eng. Perform. 30 (2021) 9403–9411, https://doi.org/10.1007/S11665-021-06112-5/METRICS.

[31] Y. Li, L. Li, J. Nie, Y. Cao, Y. Zhao, Y. Zhub, Microstructural evolution and mechanical properties of a 5052 Al alloy with gradient structures, J. Mater. Res. 32 (2017) 4443–4451, https://doi.org/10.1557/JMR.2017.310/METRICS.

[32] F. Di Gioacchino, J. Quinta da Fonseca, Plastic strain mapping with sub-micron resolution using digital image correlation, Exp. Mech. 53 (2013) 743–754, https://doi.org/10.1007/s11340-012-9685-2.

[33] J.C. Stinville, N. Vanderesse, F. Bridier, P. Bocher, T.M. Pollock, High resolution mapping of strain localization near twin boundaries in a nickel-based superalloy, Acta Mater. 98 (2015) 29–42, https://doi.org/10.1016/j.actamat.2015.07.016.

[34] Bigger R., Blaysat B., Boo C., Grewer M., Hu J., Jones A., et al. A good practices guide for digital image correlation. 2018. https://doi.org/10.32720/idics/gpg.ed1.

[35] M. Mostafavi, D.M. Collins, B. Cai, R. Bradley, R.C. Atwood, C. Reinhard, et al., Yield behavior beneath hardness indentations in ductile metals, measured by three-dimensional computed X-ray tomography and digital volume correlation, Acta Mater. 82 (2015) 468–482, https://doi.org/10.1016/j.actamat.2014.08.046.

[36] P. Neumann, Coarse slip model of fatigue, Acta Metall. 17 (1969) 1219–1225, https://doi.org/10.1016/0001-6160(69)90099-6.

[37] W. Liu, L. Yu, Y. Liu, H. Sui, H. Fan, H. Duan, Dislocation pile-up polarization model for mechanical properties of polycrystalline metals based on grain boundary resistance variability, J. Mech. Phys. Solids 160 (2022) 104793, https://doi.org/10.1016/j.jmps.2022.104793.

[38] L. Wang, J. Zhou, S. Zhang, H. Liu, S. Dong, Effect of dislocation–GB interactions on crack blunting in nanocrystalline materials, Mater. Sci. Eng.: A 592 (2014) 128–135, https://doi.org/10.1016/j.msea.2013.11.004.

[39] J.Q. Chen, H. Lu, C. Yu, J.M. Chen, M.L. Zhang, Ductility dip cracking mechanism of Ni–Cr–Fe alloy based on grain boundary energy, Sci. Technol. Weld. Join. 18 (2013) 346–353, https://doi.org/10.1179/1362171813Y.0000000113.

[40] J.W. Kysar, Energy dissipation mechanisms in ductile fracture, J. Mech. Phys. Solids 51 (2003) 795–824, https://doi.org/10.1016/S0022-5096(02)00141-2.

[41] V.V. Bulatov, B.W. Reed, M. Kumar, Grain boundary energy function for fcc metals, Acta Mater. 65 (2014) 161–175, https://doi.org/10.1016/j.actamat.2013.10.057.

[42] A.F. Bower, Applied Mechanics of Solids, 1st ed., CRC Press, 2009 https://doi.org/10.1201/9781439802489.

[43] A. Koko, T.J. Marrow, DIC2Abaqus: calculating mixed-mode stress intensity factors from 2D and 3D-stereo displacement fields, ArXiv (2025), https://doi.org/10.48550/arXiv.2409.08285.

[44] X. Su, W. Wan, F.P.E. Dunne, T.J. Marrow, Crack field analysis by optical DIC of short cracks in Zircaloy-4, Procedia Struct. Integr. 39 (2022) 663–670, https://doi.org/10.1016/j.prostr.2022.03.139.

[45] J.D. Eshelby, The force on an elastic singularity, Philos. Trans. R. Soc. Lond. Math. Phys. Sci. 244 (1951) 87–112, https://doi.org/10.1098/rsta.1951.0016.

[46] A.F. Liu, Mechanical Properties Data for Selected Aluminum Alloys. Mechanics and Mechanisms of Fracture: An Introduction, Materials Park, ASM International, Ohio, 2005, pp. 397–409.

[47] J. Vaara, A. Kunnari, T. Frondelius, Literature review of fatigue assessment methods in residual stressed state, Eng. Fail. Anal. 110 (2020) 104379, https://doi.org/10.1016/j.engfailanal.2020.104379.

[48] D.B. Marshall, B.R. Lawn, Residual stress effects in sharp contact cracking, J. Mater. Sci. 8 (14) (1979) 2001–2012, https://doi.org/10.1007/BF00551043, 1979 14.

[49] Y. Lei, N.P. O'Dowd, G.A. Webster, Fracture mechanics analysis of a crack in a residual stress field, Int. J. Fract. 106 (2000) 195–216, https://doi.org/10.1023/A:1026574400858.

[50] Y. Sumi, Computational crack path prediction for brittle fracture in welding residual stress fields, Int. J. Fract. 44 (1990) 189–207, https://doi.org/10.1007/BF00035516.